



## ISTITUTO NAZIONALE DI RICERCA METROLOGICA Repository Istituzionale

Production and characterization of  $^{111}\text{Ag}$  radioisotope for medical use in a TRIGA Mark II nuclear research reactor

This is the author's submitted version of the contribution published as:

*Original*

Production and characterization of  $^{111}\text{Ag}$  radioisotope for medical use in a TRIGA Mark II nuclear research reactor / Morselli, L.; Donzella, A.; Arzenton, A.; Asti, M.; Bortolussi, S.; Corradetti, S.; D'Agostino, G.; Di Luzio, M.; Ferrari, M.; Gandini, A.; Lunardon, M.; Villa, V.; Salvini, A.; Zangrando, L.; Zenoni, A.; Andrighetto, A.. - In: APPLIED RADIATION AND ISOTOPES. - ISSN 0969-8043. - 197:(2023).  
[10.1016/j.apradiso.2023.110798]

*Availability:*

This version is available at: 11696/79241 since: 2024-06-04T09:25:41Z

*Publisher:*

Elsevier

*Published*

DOI:10.1016/j.apradiso.2023.110798

*Terms of use:*

This article is made available under terms and conditions as specified in the corresponding bibliographic description in the repository

*Publisher copyright*

(Article begins on next page)

# Production and characterization of $^{111}\text{Ag}$ radioisotope for medical use in a TRIGA Mark II nuclear research reactor

L. Morselli<sup>a,b</sup>, A. Donzella<sup>c,d,\*</sup>, A. Arzenton<sup>a,e</sup>, M. Asti<sup>f</sup>, S. Bortolussi<sup>g,d</sup>, S. Corradetti<sup>a</sup>, G. D'Agostino<sup>h</sup>, M. Di Luzio<sup>h</sup>, M. Ferrari<sup>i,j</sup>, A. Gandini<sup>k</sup>, M. Lunardon<sup>l,m</sup>, V. Villa<sup>c,d</sup>, A. Salvini<sup>k</sup>, L. Zangrando<sup>m</sup>, A. Zenoni<sup>c,d</sup>, A. Andrichetto<sup>a</sup>

<sup>a</sup>*INFN, Laboratori Nazionali di Legnaro, Viale dell'Università 2, 35020 Legnaro, Padua, Italy*

<sup>b</sup>*Dipartimento di Fisica e Scienze della Terra, Università degli Studi di Ferrara, Via G. Saragat 1, 44121 Ferrara, Italy*

<sup>c</sup>*Dipartimento di Ingegneria Meccanica e Industriale, Università degli Studi di Brescia, Via Branze 38, 25123 Brescia, Italy*

<sup>d</sup>*INFN, Sezione di Pavia, Via A. Bassi 6, 27100 Pavia, Italy*

<sup>e</sup>*Dipartimento di Scienze Fisiche della Terra e dell'Ambiente, Università degli Studi di Siena, Via Roma 56, 53100 Siena, Italy*

<sup>f</sup>*Radiopharmaceutical Chemistry Section, Nuclear Medicine Unit, AUSL-IRCCS di Reggio Emilia, Viale Risorgimento 80, 42122 Reggio Emilia, Italy*

<sup>g</sup>*Dipartimento di Fisica, Università degli Studi di Pavia, Via A. Bassi 6, 27100 Pavia, Italy*

<sup>h</sup>*Istituto Nazionale di Ricerca Metrologica, Dipartimento di Chimica Generale, Università degli Studi di Pavia, Viale T. Taramelli 12, 27100 Pavia, Italy*

<sup>i</sup>*Laboratoire Hubert Curien, CNRS, UMR 5516, Université Jean Monnet F-42000, Saint-Etienne, France*

<sup>j</sup>*CERN - CH 1211 Geneva 23*

<sup>k</sup>*Laboratorio per l'Energia Nucleare Applicata, via G. Aselli 41, 27100 Pavia, Italy*

<sup>l</sup>*Dipartimento di Fisica ed Astronomia, Università degli Studi di Padova, Via F. Marzolo 8, 35131 Padova, Italy*

<sup>m</sup>*INFN, Sezione di Padova, Via F. Marzolo 8, 35131 Padova, Italy*

---

## Abstract

Radio Pharmaceutical Therapy (RPT) comes forth as a promising technique to treat a wide range of tumors while ensuring low collateral damage to

---

\*Corresponding author

Email address: [antonietta.donzella@unibs.it](mailto:antonietta.donzella@unibs.it) (A. Donzella)

nearby healthy tissues. This kind of cancer therapy exploits the radiation following the decay of a specific radionuclide to deliver a lethal dose to tumor tissues. In the framework of the ISOLPHARM project of INFN,  $^{111}\text{Ag}$  was recently proposed as a promising core of a therapeutic radiopharmaceutical. In this paper, the production of  $^{111}\text{Ag}$  via neutron activation of  $^{110}\text{Pd}$ -enriched samples inside a TRIGA Mark II nuclear research reactor is studied. The radioisotope production is modeled using two different Monte Carlo codes (MCNPX and PHITS) and a stand-alone inventory calculation code FISPACT-II, with different cross section data libraries. The whole process is simulated starting from an MCNP6-based reactor model producing the neutron spectrum and flux in the selected irradiation facility. Moreover, a cost-effective, robust and easy-to-use spectroscopic system, based on a Lanthanum Bromo-Chloride (LBC) inorganic scintillator, is designed and characterized, with the aim of using it, in the future, for the quality control of the ISOLPHARM irradiated targets at the SPES facility of the Legnaro National Laboratories of INFN.  $^{\text{nat}}\text{Pd}$  and  $^{110}\text{Pd}$ -enriched samples are irradiated in the reactor main irradiation facility and spectroscopically characterized using the LBC-based setup and a multiple-fit analysis procedure. Experimental results are compared with theoretical predictions of the developed models, showing that inaccuracies in the available cross section libraries prevent an accurate reproduction of the generated radioisotope activities. Models are normalized to the experimental data allowing for a reliable planning of the  $^{111}\text{Ag}$  production in a TRIGA Mark II reactor.

*Key words:* ISOLPHARM project; radiopharmaceuticals;  $^{111}\text{Ag}$ ;  $\gamma$ -spectroscopy; nuclear reactor.

---

## 1. Introduction

Neutron-rich radioisotopes that decay through  $\beta^-$  decay are among the most used agents in Radio Pharmaceutical Therapy (RPT), and their production using nuclear reactors is a well established technique [1]. Over the  
5 years, several radioisotopes were proposed as promising candidates for RPT, based on their decay characteristic (i.e. radiation type, released energy and half-life) and on the feasibility of their production.

When radioisotopes are produced for medical purposes (i.e. when they are used to prepare radiopharmaceuticals) a paramount feature of the prepa-  
10 ration is a high molar activity, as not radioactive isotopes of the sought

radionuclide can compete with it for a finite number of cellular receptors.

A promising approach for producing high-specific activity, no-carrier-added radioisotopes is offered by the Isotope Separation On-Line (ISOL) technique [2]. In this context, the ISOLPHARM project aims to study innovative radioisotopes produced through ISOL techniques at SPES [3], and, in particular, to investigate the preparation of  $^{111}\text{Ag}$ -labelled radiopharmaceuticals [4].

$^{111}\text{gAg}$  is a  $\beta^-$  emitter with an half-life of 7.5 days and contemporary emission of two  $\gamma$ -rays ( $E_\gamma=245.40(2)$  keV,  $I_\gamma = 1.24(9)\%$ ;  $E_\gamma= 342.13(2)$  keV,  $I_\gamma = 6.7(3)\%$ ) which potentially allow for SPECT imaging. Moreover, in the framework of RTP, the emission of a  $\beta^-$  having average energy of 360 keV makes it suitable for treating medium size tumors [5, 6]. Finally,  $^{111}\text{Ag}$  can be produced at SPES with good yields [7].

In the framework of the ISOLPHARM project, since the SPES ISOL facility is currently under construction, preclinical experimentation of  $^{111}\text{Ag}$ -based innovative radiopharmaceuticals will be carried out using  $^{111}\text{Ag}$  produced via the radiative neutron capture reaction at the TRIGA Mark II nuclear research reactor of the LENA Laboratory of the University of Pavia (Italy) [8]:



This reaction can lead to the formation of  $^{111}\text{Pd}$  in both its ground and isomeric states depending on the distribution of resonance states produced in the process and the  $\gamma$ -multiplicity [9]. The ground and metastable states of  $^{111}\text{Pd}$  have different half-lives, respectively 23.3 min for  $^{111}\text{gPd}$  and 5.5 h for  $^{111}\text{mPd}$ . The time-evolution of the involved nuclides can be described by the following system of ordinary differential equations:

$$\begin{cases} \frac{dN_{\text{Pd-111m}}}{dt} = -\lambda_{\text{Pd-111m}}N_{\text{Pd-111m}} + R_m N_{\text{Pd-110}} \\ \frac{dN_{\text{Pd-111g}}}{dt} = -\lambda_{\text{Pd-111g}}N_{\text{Pd-111g}} \\ \quad + B_{\text{Pd-111m} \rightarrow \text{Pd-111g}} \lambda_{\text{Pd-111m}} N_{\text{Pd-111m}} \\ \quad + R_g N_{\text{Pd-110}} \\ \frac{dN_{\text{Ag-111m}}}{dt} = -\lambda_{\text{Ag-111m}}N_{\text{Ag-111m}} + B_{\text{Pd-111g} \rightarrow \text{Ag-111m}} \lambda_{\text{Pd-111g}} N_{\text{Pd-111g}} \\ \quad + B_{\text{Pd-111m} \rightarrow \text{Ag-111m}} \lambda_{\text{Pd-111m}} N_{\text{Pd-111m}} \\ \frac{dN_{\text{Ag-111g}}}{dt} = -\lambda_{\text{Ag-111g}}N_{\text{Ag-111g}} \\ \quad + B_{\text{Ag-111m} \rightarrow \text{Ag-111g}} \lambda_{\text{Ag-111m}} N_{\text{Ag-111m}} \\ \quad + B_{\text{Pd-111g} \rightarrow \text{Ag-111g}} \lambda_{\text{Pd-111g}} N_{\text{Pd-111g}} \end{cases} \quad (2)$$

where  $\lambda_X$  is the decay constant,  $N_X$  is the number of nuclides of the X species,  $B_{X \rightarrow Y}$  is the branching ratio of the given transition,  $R_g$  and  $R_m$

are the production rate of the ground and metastable state of  $^{111}\text{Pd}$  respectively. As recently reported in [9], the cross-section favors the production of  $^{111\text{g}}\text{Pd}$  over  $^{111\text{m}}\text{Pd}$ . In particular, for the isomer production ratios, reference values for thermal and epithermal neutron fluxes are respectively:  
 35  $R_{\text{th}} = 0.0385 \pm 0.0034$  and  $R_{\text{epi}} = 0.0437 \pm 0.0046$ .

In the present paper, we present a study on the production and characterization of the  $^{111}\text{Ag}$  radioisotope in a TRIGA Mark II nuclear research reactor, for its utilization in the ISOLPHARM research activities on innovative radiopharmaceuticals. In this study, a cost-effective spectroscopic system  
 40 capable of characterizing the produced isotope is designed, constructed and tested. Thanks to its characteristics of robustness, low cost, reliability and ease of use, the realized detector system could also be used for applications in the harsh radiation environment of the SPES secondary target, where the  
 45 produced radioisotope beams will be collected [10].

The paper is organized as follows. In Section 2, the modeling of the production of the  $^{111}\text{Ag}$  radioisotope in the TRIGA Mark II nuclear reactor is described, including the procedures for the calibration of the neutron flux in the reactor irradiation facility and the Monte Carlo simulation of the  $^{\text{nat}}\text{Pd}$   
 50 and  $^{110}\text{Pd}$ -enriched sample irradiation. In Section 3, the sample irradiation procedure, the experimental set-up, the characterization and calibration of the new realized detector are described.

In Section 4, the experimental results are shown and compared with the Monte Carlo simulations of the sample irradiation process, to validate the calculations. Predictions on the possibility of producing the  $^{111}\text{Ag}$  radioisotope  
 55 in the TRIGA Mark II nuclear reactor for ISOLPHARM research activities are illustrated. In Section 5, summary and conclusions are drawn.

## 2. Modeling the production of $^{111}\text{Ag}$ in a TRIGA Mark II nuclear reactor

### 60 2.1. Modeling the irradiation facility

The TRIGA Mark II nuclear research reactor operating in Pavia is a 250 kW pool-type research reactor fueled with 20% enriched  $^{235}\text{U}$ , cooled and partly moderated with demineralized light water. The reproducibility of the reactor power is below 1%.

65 The reactor core is composed of ninety slots occupied by fuel elements, a neutron source and three control rods placed in five concentric rings around a central channel, 40 cm useful length and 26 mm diameter, used as main

irradiation facility and called Central Thimble (CT). The total neutron flux in the CT is about  $1.7 \times 10^{13}$  n/(cm<sup>2</sup>s) at full power. The reactor core is  
 70 surrounded by a graphite reflector. In Fig. 1 a horizontal cross section of the TRIGA Mark II reactor core is shown [8].

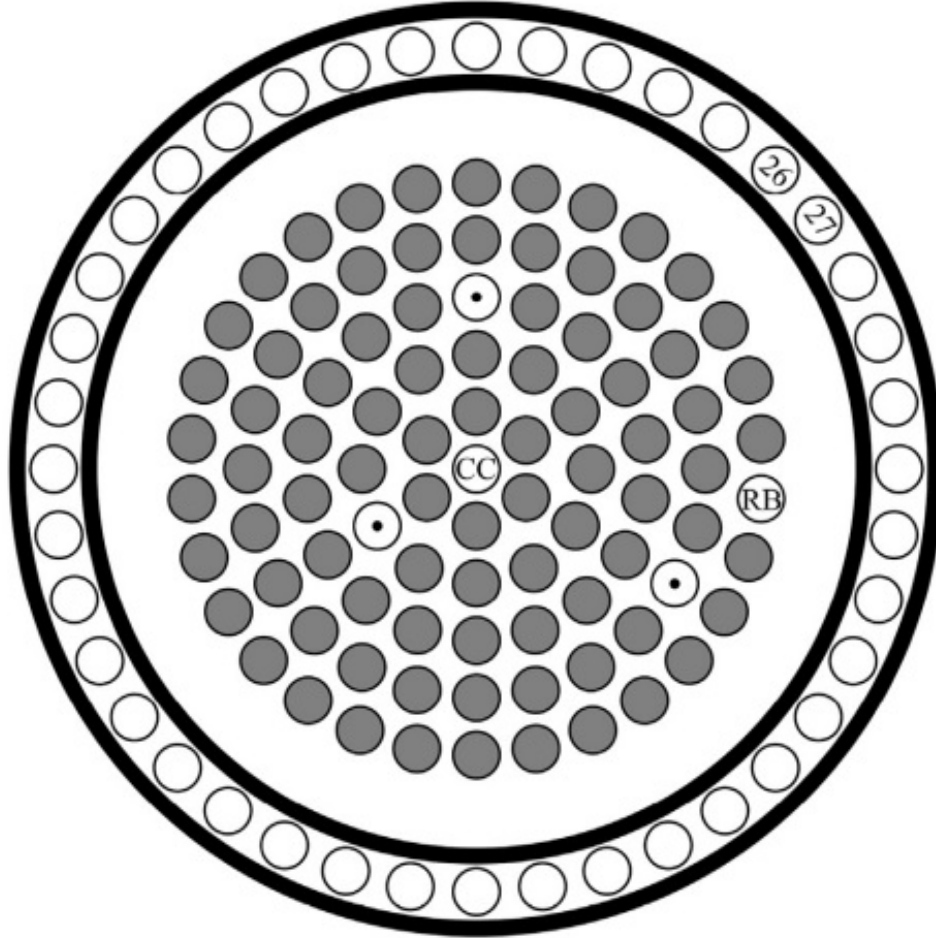


Figure 1: Horizontal cross section of the TRIGA Mark II reactor core. CC indicates the Central Thimble irradiation facility and the three pointed elements are the control rod slots. RB, 26 and 27 indicate other irradiation facilities hosted by the reactor.

A computational model of the TRIGA Mark II reactor was previously set-up for radiobiological studies performed in the thermal column [11]. For the present study, an update was necessary, and it was accomplished using

75 the Monte Carlo neutron transport code MCNP6 [12]. The new version of the TRIGA Mark II reactor model considers the re-shuffle of the fuel elements in the core described in [13], each with a corrected burnup, accounting for the functioning time of the reactor.

Simulations were carried out using the KCODE instruction, which repro-  
 80 duces the fission in the core of the reactor, starting with an external source that models an initial sampling of neutrons in the fuel bars, and letting MCNP simulate the generation of neutrons. The criticality of the system was optimized adjusting the positions of the control bars until reaching a value of the parameter  $k_{eff}$  equal to 1, with a relative error lower than 1%.

85 The calculated neutron thermal flux in the CT was compared with the available flux measurements reported in [14, 15], considered as a reference in the present study. Measurements were performed according to the Hogdahl convention [16] using Zr and Au neutron flux monitor samples, placed at different positions along the CT. Conventional thermal  $\Phi_T$  and epithermal  $\Phi_E$   
 90 neutron flux values were obtained from gamma spectra of the monitor samples. Gamma spectra were recorded with a HPGe detector, whose counting efficiency was determined using SI traceable gamma reference sources.

The measurement set-up was reproduced in the computational model including holder materials and inserts used to fix the positions of the samples.  
 95 The  $\Phi_T$  value was calculated using the F4 tally type accounting for neutrons with energies below 0.56 eV. Fig. 2 shows the comparison between the reported experimental values and the results of simulations. The relative error affecting the simulated  $\Phi_T$  lies between  $-5\%$  and  $+10\%$  up to 25 cm from the bottom of the CT, and increases up to  $+38.5\%$  at 34.5 cm.

To obtain the epithermal flux  $\Phi_E$  from the simulated results, we used the expression reported in [14]:

$$\phi_{epi}(E) = \frac{\Phi_E}{E^{1+\alpha}} \quad (3)$$

100 where  $\phi_{epi}(E)$  is the energy distribution of the epithermal flux in the epithermal range and  $\alpha$  is the parameter modeling the deviations from the  $\frac{1}{E}$  theoretical trend.

For each monitor sample, we calculated the  $\phi_{epi}(E)$  values from the neutron flux values  $\Phi_{epi}$ , simulated with a BUGE-96 binning. The  $\Phi_E$  value  
 105 was calculated as the intercept of the straight line fitted to the  $\log[\phi_{epi}(E)]$  vs  $\log(E)$  data, within the energy range comprised between 0.64 eV and  $5.2 \times 10^3$  eV.

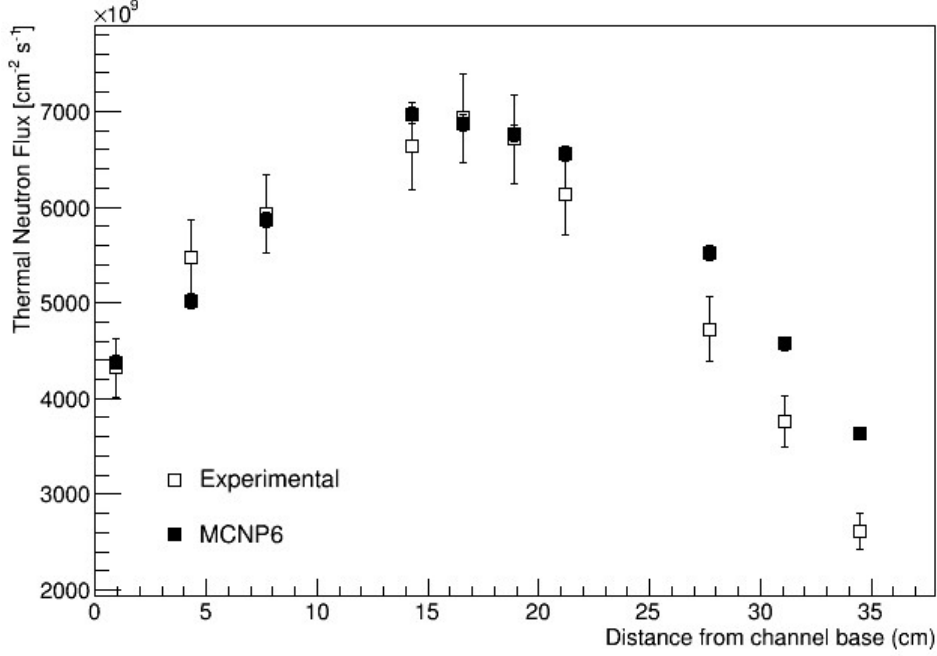


Figure 2: Comparison between experimental thermal neutron flux values (empty squares) and Monte Carlo predictions (black filled squares) along the CT. Error bars of measured and simulated data indicate a 95% confidence interval.

Fig. 3 shows the comparison between the reported experimental values and the results of simulations. The simulated  $\Phi_E$  values appear to be systematically overestimated relative to the experimental data.

The significant discrepancies affecting the simulated  $\Phi_T$  at large distance from the CT bottom and the simulated  $\Phi_E$  along all the CT required further investigations. They were mainly focused on the uncertainties affecting: the adoption of the Hogdahl convention; the modeling of dimensions and materials of the components; the calculation procedure to obtain  $\Phi_T$  and  $\Phi_E$  from simulated data.

To test the actual performance of the model, we simulated both the  $^{197}\text{Au}(n,\gamma)^{198}\text{Au}$  and  $^{94}\text{Zr}(n,\gamma)^{95}\text{Zr}$  reaction rates per target nucleus,  $RR$ . Results were compared with experimental values recorded with Au and Zr samples measured in [14].

It is worth noting that the reaction  $^{110}\text{Pd}(n,\gamma)^{111}\text{Pd}$  has a resonance integral to thermal cross section ratio,  $Q_0$ , equal to 11.9, whereas the  $Q_0$  values for  $^{197}\text{Au}(n,\gamma)^{198}\text{Au}$  and  $^{94}\text{Zr}(n,\gamma)^{95}\text{Zr}$  are 15.7 and 5.31, respectively. They

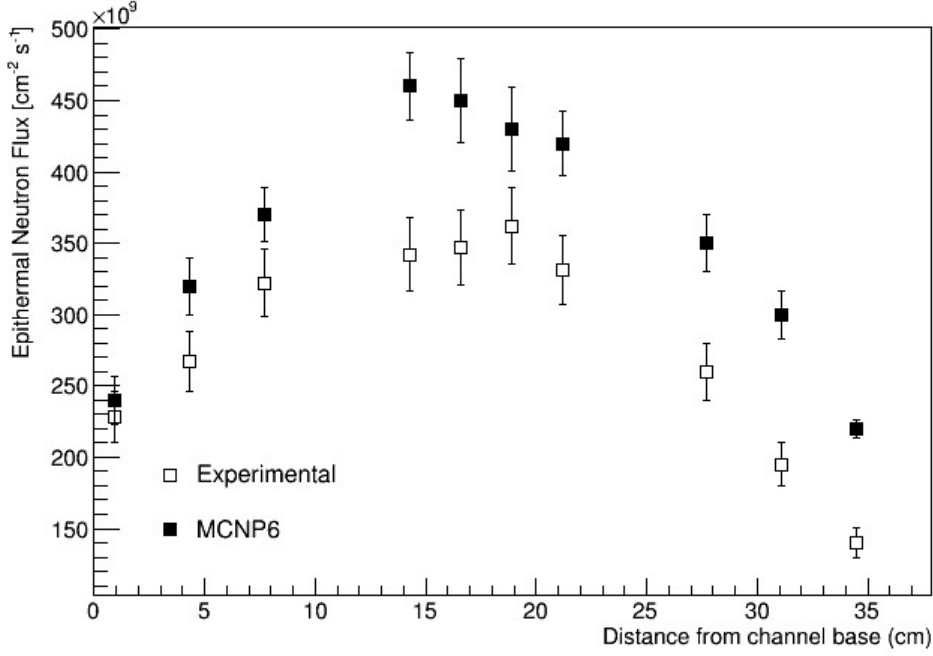


Figure 3: Comparison between experimental epithermal neutron flux values (empty squares) and Monte Carlo predictions (black filled squares) along the CT. Error bars of measured and simulated data indicate a 95% confidence interval.

are reported as recommended nuclear data in the k0 Data Base [17]. In addition, based on the Hogdahl convention,  $RR$  can be expressed as:

$$RR = \Phi_T \sigma_0 \left[ 1 + \frac{Q_0(\alpha)}{f} \right] \quad (4)$$

where  $\sigma_0$  is the thermal ( $E = 2200 \text{ m s}^{-1}$ ) neutron cross section,  $f$  is the conventional thermal to epithermal ratio  $\Phi_T/\Phi_E$ , and  $Q_0(\alpha)$  is the ratio between the resonance integral and  $\sigma_0$ , for a  $1/E^{(1+\alpha)}$  neutron spectrum in the epithermal region.

125 Accordingly, the contribution to  $RR$  due to the thermal and epithermal neutron flux for  $^{110}\text{Pd}$  is close to the contribution for  $^{197}\text{Au}$  and  $^{94}\text{Zr}$ . Thus, the comparison carried out with  $^{197}\text{Au}$  and  $^{94}\text{Zr}$  is meaningful to check the suitability of the computational model also for  $^{110}\text{Pd}$ .

130 Results for the comparisons of experimental and simulated  $RR$  per target nucleus, for  $^{197}\text{Au}$  and  $^{94}\text{Zr}$  respectively, are shown in Fig. 4 and Fig. 5.  $RR$  are plotted versus the distance of the sample from the bottom of the CT.

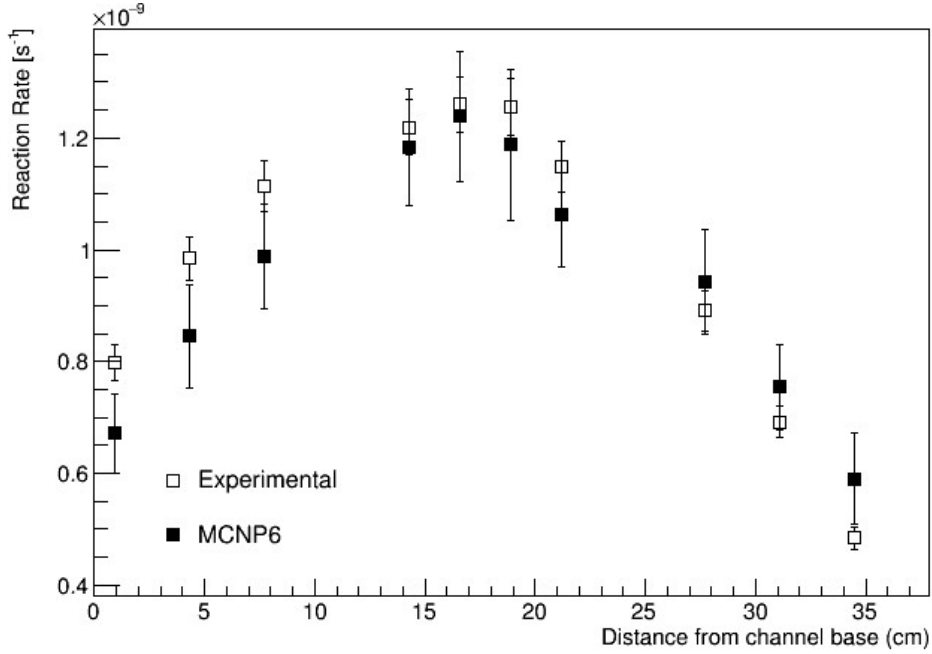


Figure 4: Comparison between the experimental  $RR$  (empty squares) and simulated  $RR$  (filled black squares) for  $^{197}\text{Au}(n,\gamma)^{198}\text{Au}$  in Au samples. Values are expressed per target nucleus; error bars of measured and simulated data indicate a 95% confidence interval.

The relative error affecting the simulated  $^{197}\text{Au}$   $RR$  values lies between  $-16.0\%$ , at 0.9 cm from the bottom of the CT, and  $+23.0\%$  at 34.5 cm. For the simulated  $^{94}\text{Zr}$   $RR$  values, it lies between  $-11.5\%$  at 31.1 cm and  $+45.7\%$  at 34.5 cm. In both cases, the best results are obtained close to the middle vertical position, for example at 14.3 cm, 16.6 cm, 18.9 cm and 21.2 cm from the bottom of the CT. In these positions, the relative error lies between  $-8.0\%$  and  $+6.5\%$ . Effects on  $RR$  of the significant discrepancies observed for  $\Phi_E$  (see Fig. 3) are limited by the low percentage of epithermal neutron flux contributing to the reactions.

Finally, these results show that the updated TRIGA Mark II reactor model reproduces the thermal and epithermal neutron fluxes in a reliable way, in positions of the CT comprised between about 14 cm and 22 cm from the bottom of the CT, with an error less than 10%.

In Fig. 6 the simulated neutron spectrum of the TRIGA Mark II reactor is shown. It includes the thermal, epithermal and fast components in the energy range between  $1 \times 10^{-9}$  MeV and 20 MeV, expressed in neutron/(cm<sup>2</sup>s<sup>-1</sup>)

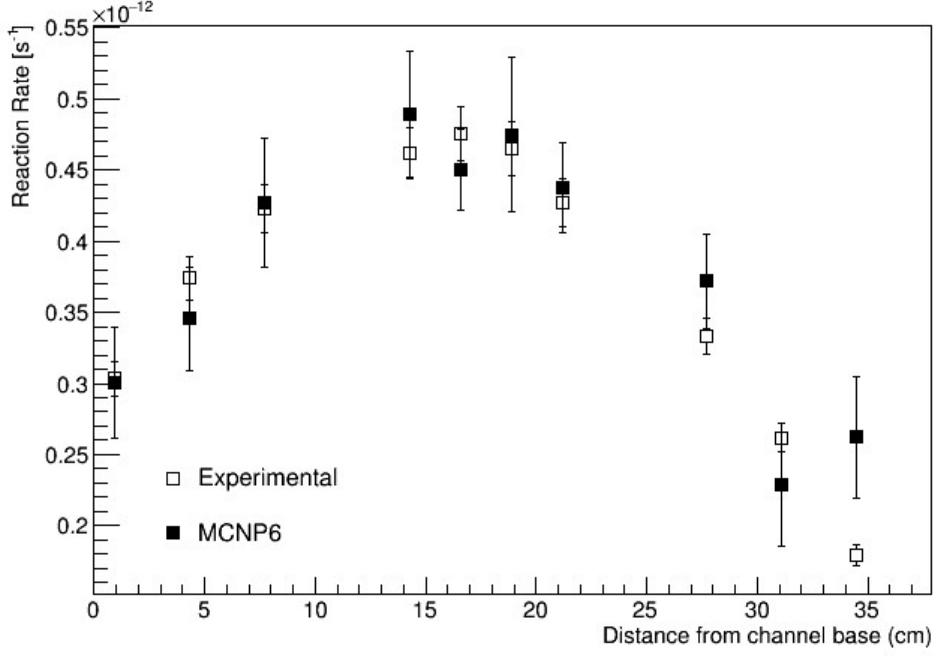


Figure 5: Comparison between the experimental  $RR$  (empty squares) and simulated  $RR$  (filled black squares) for  $^{94}\text{Zr}(n,\gamma)^{95}\text{Zr}$  in Zr samples. Values are expressed per target nucleus; error bars of measured and simulated data indicate a 95% confidence interval.

per unit lethargy. The spectrum is calculated at the same position where the palladium samples are placed in the CT irradiation facility, at about 17 cm from the bottom of the CT. The spectrum is calculated in 709 group-energy bins with the described MCNP6 model of the reactor. In the following paragraph, this spectrum is used to model the palladium irradiation process with radioisotope formation and successive decay.

## 2.2. Modeling the palladium sample irradiation

Two Monte Carlo calculation tools, MCNPX (v2.7.0) [18] and PHITS (v3.27) [19], are employed to model the irradiation of the palladium samples placed in the CT irradiation facility.

With both tools, a very simplified geometrical set-up is modeled, including a 100 mg palladium sample, the sample aluminum holder, the CT cylindrical cavity filled with air at NTP, surrounded by a cylindrical cell of the same size as the reactor core volume. Inside the latter volume, an isotropic neutron source with the same spectrum as the one reported in Fig. 6 is uni-

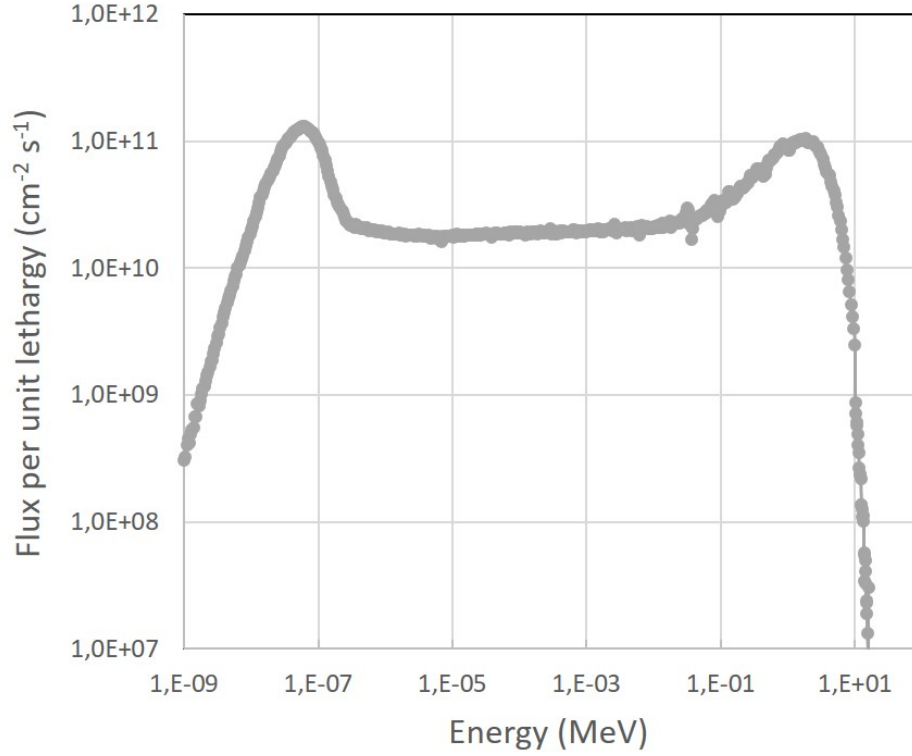


Figure 6: Simulated neutron spectrum at about 17 cm from the bottom of the in the CT irradiation facility. The Monte Carlo statistical error is of the order of 1%.

formly generated. Results of the simulation are normalized to the expected value of the neutron flux on the target holder at 250 kW reactor full power.

165 MCNPX and PHITS simulate the irradiation process and the isotope formation during the irradiation phase. In order to predict the radioisotope formation and decay at different times during the irradiation period and in the following cooling phase, MCNPX is interfaced with CINDER'90 [20], a nuclide evolution program, whereas PHITS makes use of the internal DCHAIN  
170 utility [21] to perform the same operation.

A supplementary calculation of the palladium sample activation, with subsequent nuclide evolution at different times, is performed with FISPACT-II [22], a stand-alone enhanced multiphysics inventory code. The same neutron flux as with the two previous Monte Carlo calculation tools is employed.

175 To model the interactions of the low-energy neutrons produced by the

reactor in the palladium samples and the time evolution of the generated radioisotopes, some different cross-section data libraries and decay data files are implemented in the simulation programs. Indeed, as discussed in Section 4, different libraries contain sometimes rather different cross section data for the same reactions or do not include cross sections for relevant metastable states.

Two types of palladium samples are considered in the simulations:  $^{\text{nat}}\text{Pd}$  and  $^{110}\text{Pd}$ -enriched samples. In the experimental part of this work, described in Section 3, both types of samples are irradiated.

$^{\text{nat}}\text{Pd}$  samples are mainly used for testing the procedures of irradiation and characterization.  $^{110}\text{Pd}$ -enriched samples are needed to maximize the  $^{111}\text{Ag}$  production, reducing, at the same time, the production of the undesired  $^{109}\text{Pd}$  radioisotope. Indeed, the latter is produced via neutron capture on the  $^{108}\text{Pd}$  stable isotope and quickly decays into the stable isotope  $^{109}\text{Ag}$ , impossible to be chemically separated from the desired  $^{111}\text{Ag}$ . Therefore, if present in abundance, it may definitely compromise the specific activity of the produced  $^{111}\text{Ag}$ .

The isotopic compositions of the  $^{\text{nat}}\text{Pd}$  sample and of the  $^{110}\text{Pd}$ -enriched sample are reported in Table 1.

Isotope	$^{\text{nat}}\text{Pd}$	$^{110}\text{Pd}$ -enriched
$^{102}\text{Pd}$	$(1.02 \pm 0.01)\%$	0.01%
$^{104}\text{Pd}$	$(11.14 \pm 0.08)\%$	0.05%
$^{105}\text{Pd}$	$(22.33 \pm 0.08)\%$	0.09%
$^{106}\text{Pd}$	$(27.33 \pm 0.03)\%$	0.13%
$^{108}\text{Pd}$	$(26.46 \pm 0.09)\%$	0.33%
$^{110}\text{Pd}$	$(11.72 \pm 0.09)\%$	$(99.4 \pm 0.10)\%$

Table 1: Isotopic composition of  $^{\text{nat}}\text{Pd}$  and  $^{110}\text{Pd}$ -enriched samples.

### 3. Palladium irradiation and characterization.

#### 3.1. Palladium sample irradiation

The experiment is performed irradiating, at the same time and in the same polyethylene holder, a 62.7 mg  $^{110}\text{Pd}$ -enriched and a 60.7 mg  $^{\text{nat}}\text{Pd}$  sample. Both samples are irradiated for one hour inside the CT at the full

200 reactor power of 250 kW. They are placed at about 17 cm from the CT bottom, approximately at the center of the reactor core.

After the end of the irradiation, the samples cool down for 2.5 hours prior to the start of the spectroscopic measurements. The  $^{110}\text{Pd}$ -enriched sample is measured for 21 hours, whereas the  $^{\text{nat}}\text{Pd}$  sample is measured for 20 minutes  
205 immediately after the end of the  $^{110}\text{Pd}$ -enriched sample measurement.

The  $^{\text{nat}}\text{Pd}$  sample is measured to perform a consistency check of the measurement procedure. In fact, the ratio between the measured activities of  $^{111}\text{Ag}$  in the two samples,  $R_{\text{Ag}111}$ , must be equal to the ratio between the amounts of  $^{110}\text{Pd}$  contained in the two samples,  $R_{\text{Pd}110}$ .

### 210 3.2. Experimental Setup

*Instrumentation.* The samples are characterized using a spectroscopic system designed for the quality control of the ISOLPHARM collection target system at the SPES facility [10]. The requirements of the designed detector system are the following:

- 215 • to be able to sustain high acquisition rates with negligible dead time, since high activities are expected;
- to have a good energy resolution (e.g. between 3% and 4% at 661 keV) allowing for a reliable spectroscopic characterization of the samples;
- to be compact, portable and easy to use; indeed, it is intended to be  
220 also used in experimental activities correlated with the ISOLPHARM project (i.e. ex-vivo biodistribution studies [23]).

The proposed system is based on a Lanthanum Bromo-Chloride (LBC) inorganic scintillator detector. The choice represents a cost-effective solution with respect to the standard use of HPGe detectors. Indeed, considering  
225 its aim, high resolution is not mandatory, since only isobaric beams will be deposited onto the aforementioned collection targets and thus the acquired  $\gamma$ -spectra should be populated by only a few separated peaks. This crystal exhibits an intrinsic background, similar to the one of the Lanthanum Bromide ( $\text{LaBr}_3$ ) detectors [24], that does not represent a concern for high rate  
230 measurements.

The selected LBC crystal has a cylindrical shape, with 1 inch (2.54 cm) diameter and 1 inch height, encapsulated in a dedicated aluminum case due to the crystal hygroscopicity. The crystal is coupled with a R6231 PMT having

a superbialkali photo-cathode manufactured by HAMAMATSU. The whole  
 235 assembly is enclosed in a custom designed plastic case realized using plastic  
 additive manufacturing. Since irradiated samples are transported inside a  
 3 mL plastic vial, a dedicated support is also designed in order to ensure a  
 well defined distance between the detector and the sample to be measured  
 (see Fig. 7a).

240 To provide an additional check on the characterization and calibration  
 of the new LBC detector, the same  $^{110}\text{Pd}$ -enriched sample, irradiated in the  
 same conditions in a different experiment, was measured using an HPGe  
 detector. The adopted REGe<sup>TM</sup> detector is an n-type Reverse Electrode Ger-  
 manium detector manufactured by Mirion Technologies. The spectroscopic  
 245 measurement started 16 hours after the end of the irradiation.

*LBC Data Acquisition System.* The PMT anode signal is digitized using a  
 CAEN DT-5725 digitizer, while the PMT voltage (operated at  $-650$  V) is  
 supplied using an USB powered desktop HV power supply manufactured by  
 CAEN (DT-5470). The Digital Pulse Processing (DPP) firmware is flashed  
 250 on the digitizer FPGA which provided on-line, for each event, the relative  
 timestamp alongside the complete integration of the signal (Long Gate).

In order to enhance the energy resolution of the setup, the relevant DPP  
 parameters are optimized making it possible to reach an energy resolution of  
 3.08% at 661.6 keV.

255 The acquisition is controlled using the ABCD (Acquisition and Broadcast  
 of Collected Data) open source software [25, 26].

*LBC Detector Efficiency.* The detector absolute full energy peak efficiency  
 is evaluated through a Monte Carlo simulation of the detector implemented  
 using the GEANT4 toolkit [27]. The whole detector geometry is built in  
 260 GEANT4 starting from the constructive CAD drawings using the CADMesh  
 library [28] (see Fig. 7b).

The simulation is validated with measurements using  $^{60}\text{Co}$ ,  $^{133}\text{Ba}$ ,  $^{137}\text{Cs}$ ,  
 and  $^{152}\text{Eu}$  and  $^{241}\text{Am}$   $\gamma$ -calibration sources. The graph of Fig. 8 shows a  
 good agreement between the experimental values and the MC simulation  
 265 up to 1.5 MeV. All the simulations were run by means of the CloudVeneto  
 private Cloud infrastructure [29].

## 4. Results

### 4.1. Measurement of $^{111}\text{Ag}$ and $^{111\text{m}}\text{Pd}$ activities

In Fig. 9, the  $\gamma$ -ray spectra obtained 5 hours after the end of the irradiation by the measurement, respectively, of a  $^{\text{nat}}\text{Pd}$  sample and an  $^{110}\text{Pd}$ -enriched one are shown. As expected, the  $\gamma$ -rays associated with the decay of  $^{111}\text{Ag}$  are more evident in the spectrum taken with the  $^{110}\text{Pd}$ -enriched sample, given the larger amount of  $^{110}\text{Pd}$  contained. In the following, we focus on the data collected with the  $^{110}\text{Pd}$ -enriched sample and on two  $\gamma$  transitions of the produced radioisotopes: 342 keV for  $^{111}\text{Ag}$  and 391 keV for  $^{111\text{m}}\text{Pd}$  respectively.

The activity A, in Bequerels, extrapolated from a specific gamma transition, is obtained from the relation:

$$A = \frac{N}{\varepsilon \cdot B_{\gamma} \cdot T} \quad (5)$$

where N is the number of counts under the peak associated to a given transition,  $\varepsilon$  is the absolute detection efficiency,  $B_{\gamma}$  is the transition branching ratio and T is the acquisition time in seconds.

To obtain the number of events N associated with a specific transition during a given time T, data are split into 20-minute long batches from which energy spectra are obtained. From each spectrum, the environmental plus intrinsic background is subtracted using a long acquisition without any sample.

Due to the great number of transition peaks present in the spectra and the limited energy resolution of the LBC detector, a fit procedure considering only a single peak plus exponential background at a time, turns out to be rather ineffective and unstable.

For this reason, a simultaneous multiple fit procedure on the full spectrum is adopted. In Table 2, the list of the main  $\gamma$  transition energies and branching ratios present in the measured spectra, in the region of interest between 290 keV and 500 keV, is shown. Data are taken from NDS [30, 31].

Each subtracted spectrum is fitted, between 290 keV and 500 keV, with the following formula:

$$f(E) = ae^{-bE} + \sum_{E_i \in \{E_1, \dots, E_n\}} \frac{A_{E_i}}{\sqrt{2\pi}\sigma_{E_i}} e^{-\frac{1}{2} \left( \frac{E-E_i}{\sigma_{E_i}} \right)^2} \quad (6)$$

Nuclide	$E_i$ [keV]	$B_\gamma$ [%]
$^{109}\text{Pd}$	309	$0.00424 \pm 0.00013$
	311	$0.0338 \pm 0.0009$
	413	$0.00718 \pm 0.00021$
	415	$0.0114 \pm 0.0003$
$^{111\text{m}}\text{Pd}$	309	$0.00424 \pm 0.00013$
	358	$0.44 \pm 0.06$
	376	$0.92 \pm 0.15$
	<b>391</b>	<b><math>5.7 \pm 0.7</math></b>
	413	$1.9 \pm 0.5$
	415	$1.7 \pm 0.4$
	439	$0.25 \pm 0.05$
	444	$0.132 \pm 0.019$
	454	$0.27 \pm 0.11$
$^{111}\text{Ag}$	<b>342</b>	<b><math>6.7 \pm 0.3</math></b>

Table 2: List of all the  $\gamma$  peaks considered in the multiple fit procedure [30, 31]. In bold character the two  $\gamma$  transitions studied.

where  $E_i$  are the peak energies,  $A_{E_i}$  are the peak areas in the spectrum and  $\sigma_{E_i}$  are the standard deviations of the peaks. The exponential term represents the physical background in the spectrum measurement, where  $a$  and  $b$  are free parameters.

In order to reduce the degrees of freedom of the function, the fit is done by fixing all the peak energies within the fitting region at the values reported in Table 2. The standard deviation of the 342 keV peak is left as a free parameter, while the standard deviations of the all the other peaks are appropriately scaled using the following relation:

$$\sigma(E_i) = \sigma_{342} \cdot \sqrt{\frac{E_i}{E_{342}}} \quad (7)$$

Since the estimation of the background term is largely reliant on the fit energy limits, the fit is repeated a number of times for each spectrum by systematically varying the minimum and maximum energy limits. The obtained distributions of the free parameters allowed the systematic error

associated with the fit technique to be estimated as the standard deviations of the distributions themselves.

Energy spectra from 20-minute long data batches collected at different times after the end of the irradiation are analyzed with the described procedure. The result of the multiple fits of the spectra allowed the values of the peak areas  $A_{E_i}$  to be extracted at different times for the two  $\gamma$  transitions under study: 342 keV for  $^{111}\text{Ag}$  and 391 keV for  $^{111\text{m}}\text{Pd}$  respectively. From the peak areas the contained number of events  $N$  is extracted and the  $^{111}\text{Ag}$  and  $^{111\text{m}}\text{Pd}$  activities are calculated at different times with Eq. 5.

The experimental results are reported in Fig. 10, where the activities of the two analyzed isotopes, measured with the LBC detector, are reported at different times after the beginning of the irradiation. The error bars account both for the statistical error and for the systematic error of the multiple fit procedure. In the same plot, the isotope activities measured with the HPGe detector in another equivalent experiment, for the same  $^{110}\text{Pd}$ -enriched sample, are reported too. The latter measurements started 16 hours after the end of the irradiation. The solid lines are the solution of the system of ordinary differential equations of Eq. 2 with  $R_{\text{metastable}}/R_{\text{ground}}=4\%$

From Fig. 10 some conclusions can be drawn. First, the absolute value of the  $^{111}\text{Ag}$  and  $^{111\text{m}}\text{Pd}$  activities measured with the LBC detector, using the simultaneous multiple fit procedure, and with the HPGe detector, are in very good agreement. This confirms the accuracy of the LBC detector calibration and characterization and the effectiveness of the analysis procedure.

Second, the measured yields of  $^{111\text{m}}\text{Pd}$  and  $^{111}\text{Ag}$  are compatible with the production rate ratio between the metastable and the ground state of  $^{111}\text{Pd}$ , as reported in [9]. Indeed, the solution of the system of Eq. 2 is calculated with the ratio between  $R_m$  and  $R_g$  constrained to be 4%. The curves interpolate correctly the data also at short times after the beginning of the irradiation, where the balance of the ground and metastable states of  $^{111}\text{Pd}$ , which have very different half-lives, manifests itself in the data behavior. Moreover, the measured exponential decays of the two radioisotopes  $^{111}\text{Ag}$  and  $^{111\text{m}}\text{Pd}$  are well in agreement with the reference half-lives, 7.5 days and 5.5 hours, respectively.

Finally, it is demonstrated that the irradiation of a  $^{110}\text{Pd}$ -enriched sample of 62.7 mg during one hour in the TRIGA Mark II reactor CT, at full power, can produce  $122 \pm 5 \mu\text{Ci}$  of  $^{111}\text{Ag}$  and  $110 \pm 13 \mu\text{Ci}$  of  $^{111\text{m}}\text{Pd}$ , 3.5 hours after the beginning of the irradiation. This result allows a reliable planning of the  $^{111}\text{Ag}$  production for the use in the ISOLPHARM project to be performed.

#### 4.2. Measurement of the $^{110}\text{Pd}$ isotopic ratio

340 As reported in Section 3.1, the  $^{\text{nat}}\text{Pd}$  sample is irradiated and measured to check the consistency of the measurement and of the analysis procedure. In fact, the ratio between the measured activities of  $^{111}\text{Ag}$  in the  $^{\text{nat}}\text{Pd}$  and  $^{110}\text{Pd}$ -enriched samples,  $R_{\text{Ag}111}$ , must be equal to the ratio between the amounts of  $^{110}\text{Pd}$  contained in the two samples,  $R_{\text{Pd}110}$ .

345 The measured value  $R_{\text{Ag}111} = (11.7 \pm 0.5)\%$  is found to be compatible with the reference  $R_{\text{Pd}110} = (11.8 \pm 0.14)\%$  obtained by Table 1.

#### 4.3. Comparison with model predictions

The present experimental results are compared with the predictions obtained with the model of the palladium sample irradiation process described in Section 2. In Fig. 11, the activity of  $^{111}\text{Ag}$ , measured both with LBC and HPGe detectors as a function of the elapsed time after the beginning of the irradiation, is compared with the predictions of Monte Carlo simulations. Experimental and theoretical values are normalized to a 100 mg  $^{110}\text{Pd}$ -enriched sample.

355 As illustrated in Section 2, simulations of the process are performed with MCNPX and PHITS. In addition, a calculation of the  $^{111}\text{Ag}$  produced activity is performed with the inventory simulation code FISPACT-II. The neutron flux in the CT calculated by the updated model of the TRIGA Mark II reactor, and shown in Fig. 6, is used. All calculations are performed with different sets of cross section libraries. From Fig. 2, 4 and 5, the systematic error associated to the modeling of the neutron flux is estimated to be less than 10%.

Fig. 11 shows that no combination of calculation tool and cross section library reproduces satisfactorily the absolute values of the experimental data. Data are indeed positioned between the theoretical predictions of MCNPX with EAF-2010 and CINDER'90 data library (blu curve) (+ 25%), and PHITS with JENDL-4.0 (brown curve) (−40%) and FENDL/A-3.0 (orange curve) (−70%). Moreover, theoretical predictions of PHITS with FENDL/A-3.0 do not reproduce the data behavior at short times after the beginning of the irradiation, where the balance of the ground and metastable states of  $^{111}\text{Pd}$  determines the slope of the curve.

370 The use of the same calculation tool with different cross section libraries, as PHITS with JENDL-4.0 and FENDL/A-3.0, produces predictions with large differences. Conversely, the use of the same cross section library,

375 JENDL-4.0, with different calculation tools as PHITS and FISPACT-II (violet curve) produces comparable predictions. Finally, FISPACT-II with the TENDL-2019 cross section libraries (green curve), provides the best approximation to the experimental data.

Hence, we can conclude that the disagreement between the different model  
 380 predictions and the experimental data is likely due to inaccuracies in the available cross section libraries. Nevertheless, based on the presented results, the predictions of the model can be normalized to the experimental data in order to confidently plan the  $^{111}\text{Ag}$  production in the TRIGA Mark II reactor for use in the ISOLPHARM project activities.

#### 385 4.4. Prediction of the $^{111}\text{Ag}$ production at the TRIGA Mark II reactor

In Fig. 12, the prediction of the activities of three generated radioisotopes,  $^{111\text{g}}\text{Pd}$  (pink curve),  $^{111\text{m}}\text{Pd}$  (violet curve) and  $^{111}\text{Ag}$  (green curve) is shown. They are produced in a three-day irradiation of a 100 mg  $^{110}\text{Pd}$ -enriched sample in the CT of the TRIGA Mark II reactor at full power. The activities  
 390 are plotted as a function of the time after the beginning of the irradiation. A duty cycle of the TRIGA Mark II reactor of 6 hours irradiation a day is assumed, compatible with the LENA laboratory standard operations, during three days.

Calculations are performed using FISPACT-II with the the TENDL-2019  
 395 cross section library. In agreement with the results of Section 4.3, this combination of tools provides the best approximation to the experimental data. Moreover, TENDL-2019 is the most recent and most complete cross section library available. Theoretical predictions should underestimate the effective  $^{111}\text{Ag}$  production by about 25%.

400 For these reasons, we can confidently expect that the production of  $^{111}\text{Ag}$  by irradiation of  $^{110}\text{Pd}$ -enriched samples in the TRIGA Mark II reactor may amount to about 1 mCi per day per 100 mg of irradiated material during a few days.

## 5. Summary and conclusions

405 In the present paper a study of the production and characterization of  $^{111}\text{Ag}$  radioisotope for medical use in a TRIGA Mark II nuclear research reactor, via the neutron capture reaction on  $^{110}\text{Pd}$  of Eq. 1, is performed.

The model of the TRIGA Mark II reactor of the LENA laboratory of the University of Pavia, Italy, is updated to match experimental data on

410 the measured neutron flux in the reactor CT irradiation facility. A model of the irradiation process of  $^{nat}\text{Pd}$  and  $^{110}\text{Pd}$ -enriched samples in the CT irradiation facility is developed by means of MCNPX, PHITS and FISPACT-II calculation tools and different cross section libraries.

For the characterization of the irradiated palladium samples, a new detector system based on a Lanthanum Bromo-Chloride (LBC) inorganic scintillator is designed and constructed. The detector system features high acquisition rate, good energy resolution, compactness, portability and ease to use. It is a satisfactory cost-effective solution with respect to the standard represented by HPGe detectors. The LBC detector is intended to be employed in the harsh radiation environment of the SPES secondary collection target system.

420 The test of the new LBC detector system is performed measuring the spectra of  $^{nat}\text{Pd}$  and  $^{110}\text{Pd}$ -enriched samples after one hour irradiation in the CT irradiation facility of the TRIGA Mark II reactor. A simultaneous multiple fit procedure is developed for the analysis of the spectra. Results for the measured activities of the main radioisotopes generated during the irradiation are in good agreement with measurements performed with a HPGe detector and with the reference value of the  $^{111}\text{Pd}$  isomer production ratios.

425 Comparison of the experimental results obtained for one hour irradiation with the predictions of the models shows that inaccuracies in the cross section libraries prevent the accurate reproduction of the experimental values of the produced  $^{111}\text{Ag}$  activity. Nevertheless, the model predictions can be normalized to the obtained experimental values. Therefore, reliable estimations of the production of the  $^{111}\text{Ag}$  isotope in the TRIGA Mark II reactor can be obtained, with the aim of testing innovative radiopharmaceuticals based on  $^{111}\text{Ag}$  in the ISOLPHARM project.

## Acknowledgements

This research was carried out in the framework of the ISOLPHARM\_EIRA experiment, supported by INFN, aimed at the design and characterization of innovative radiopharmaceuticals based on the  $^{111}\text{Ag}$  radioisotope.

## 440 References

- [1] S. Mirzadeh, L. Mausner, M. A. Garland, Reactor-produced medical radionuclides, Handbook of nuclear chemistry (2011) 1857.

- 445 [2] R. M. dos Santos Augusto, L. Buehler, Z. Lawson, S. Marzari, M. Stachura, T. Stora, C.-M. collaboration, et al., CERN-MEDICIS (medical isotopes collected from ISOLDE): a new facility, *Applied Sciences* 4 (2) (2014) 265–281.
- 450 [3] A. Andrichetto, M. Tosato, M. Ballan, S. Corradetti, F. Borgna, V. Di Marco, G. Marzaro, N. Realdon, The ISOLPHARM project: ISOL-based production of radionuclides for medical applications, *Journal of Radioanalytical and Nuclear Chemistry* 322 (1) (2019) 73–77.
- 455 [4] M. Ballan, M. Tosato, M. Verona, M. Caeran, F. Borgna, E. Vettorato, S. Corradetti, L. Zangrando, M. Sgaravatto, M. Verlato, et al., Preliminary evaluation of the production of non-carrier added  $^{111}\text{Ag}$  as core of a therapeutic radiopharmaceutical in the framework of ISOLPHARM<sub>Ag</sub> experiment, *Applied Radiation and Isotopes* 164 (2020) 109258.
- [5] P. A. Schubiger, A. Smith, Optimising the radioimmunotherapy of malignant disease: the broadening choice of carrier and effector moieties, *Pharmaceutica Acta Helveticae* 70 (3) (1995) 203–217.
- 460 [6] A. Vértes, S. Nagy, Z. Klencsár, R. G. Lovas, F. Rösch, *Handbook of nuclear chemistry*, Vol. 4, Springer, 2003.
- [7] A. Monetti, A. Andrichetto, C. Petrovich, M. Manzolaro, S. Corradetti, D. Scarpa, F. Rossetto, F. M. Dominguez, J. Vasquez, M. Rossignoli, et al., The RIB production target for the SPES project, *The European Physical Journal A* 51 (10) (2015) 1–11.
- 465 [8] M. Prata, D. Alloni, P. De Felice, M. Palomba, A. Pietropaolo, M. Pillon, L. Quintieri, A. Santagata, P. Valente, Italian neutron sources, *The European Physical Journal Plus* 129 (11) (2014) 1–15.
- [9] K. Krane, Neutron capture cross sections of Pd 108, 110, *Physical Review C* 99 (4) (2019) 044313.
- 470 [10] M. Ballan, E. Vettorato, L. Morselli, M. Tosato, S. Nardella, F. Borgna, S. Corradetti, A. Monetti, M. Lunardon, A. Zenoni, et al., Development of implantation substrates for the collection of radionuclides of medical interest produced via ISOL technique at INFN-LNL, *Applied Radiation and Isotopes* 175 (2021) 109795.

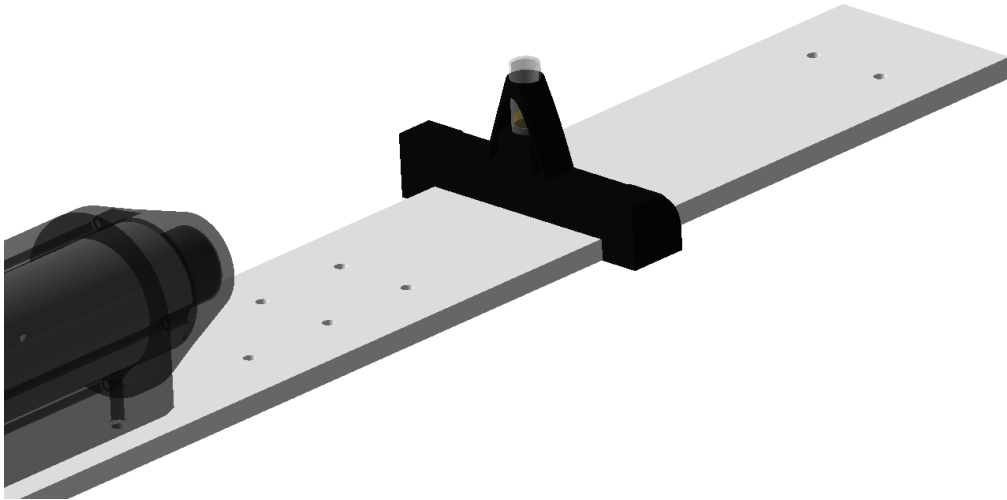
- 475 [11] S. Bortolussi, N. Protti, M. Ferrari, I. Postuma, S. Fatemi, M. Prata,  
F. Ballarini, M. Carante, R. Farias, S. González, M. Marrale, S. Gallo,  
A. Bartolotta, G. Iacoviello, D. Nigg, S. Altieri, Neutron flux and gamma  
dose measurement in the BNCT irradiation facility at the TRIGA re-  
actor of the University of Pavia, Nuclear Instruments and Methods in  
480 Physics Research B 414 (2018) 113–120.
- [12] T. Goorley, MCNP6. 1.1-beta release notes, Tech. rep., LA-UR-14-24680  
(2014).
- [13] D. Chiesa, M. Clemenza, S. Pozzi, E. Previtali, M. Sisti, D. Alloni,  
G. Magrotti, S. Manera, M. Prata, A. Salvini, A. Cammi, M. Zanetti,  
485 A. Sartori, Fuel burnup analysis of the TRIGA Mark II reactor at the  
University of Pavia, Annals of Nuclear Energy 96 (2016) 270–276.
- [14] M. Di Luzio, M. Oddone, M. Prata, D. Alloni, G. D’Agostino, Measure-  
ment of the neutron flux parameters  $f$  and  $\alpha$  at the Pavia TRIGA Mark  
II reactor, Journal of Radioanalytical and Nuclear Chemistry 312 (1)  
490 (2017) 75–80.
- [15] M. Di Luzio, G. D’Agostino, M. Oddone, A. Salvini, Vertical variations  
of flux parameters in irradiation channels at the TRIGA Mark II reactor  
of Pavia, Progress in Nuclear Energy 113 (2019) 247–254.
- [16] T. Høgdahl, Neutron absorbtion in pile neutron analysis, Tech. rep.,  
495 MMPP-226-1 (1962).
- [17] Nuclear Data SC Data Base (2020).  
URL [http://www.kayzero.com/k0naa/k0naaorg/Nuclear\\_Data\\_SC/  
Entries/2020/8/24\\_Update\\_of\\_k0-database\\_I-128.html](http://www.kayzero.com/k0naa/k0naaorg/Nuclear_Data_SC/Entries/2020/8/24_Update_of_k0-database_I-128.html)
- [18] D. B. Pelowitz, J. W. Durkee, J. S. Elson, M. L. Fensin, J. S. Hen-  
500 dricks, M. R. James, R. C. Johns, G. W. McKinney, S. G. Mashnik,  
J. M. Verbeke, et al., MCNPX 2.7. 0 Extensions, Los Alamos National  
Laboratory, Los Alamos, NM, LA-UR-11-02295 4 (2011).
- [19] T. Sato, Y. Iwamoto, S. Hashimoto, T. Ogawa, T. Furuta, S.-i. Abe,  
505 T. Kai, P.-E. Tsai, N. Matsuda, H. Iwase, N. Shigyo, L. Sihver, K. Ni-  
ita, Features of Particle and Heavy Ion Transport code System(PHITS)  
version 3.02, Journal of Nuclear Science and Technology 55 (6) (2018)  
684–690.

- [20] F. X. Gallmeier, P. D. Ferguson, W. Lu, E. B. Iverson, G. Muhrer, S. T. Holloway, C. Kelsey, E. Pitcher, M. Wohlmuther, B. J. Micklich, The CINDER'90 transmutation code package for use in accelerator applications in combination with MCNPX (2010).  
URL <https://www.osti.gov/biblio/1027400>
- [21] H. N. Ratliff, N. Matsuda, S. ichiro Abe, T. Miura, T. Furuta, Y. Iwamoto, T. Sato, Modernization of the DCHAIN-PHITS activation code with new features and updated data libraries, Nuclear Instruments and Methods in Physics Research Section B: Beam Interactions with Materials and Atoms 484 (2020) 29–41.
- [22] J.-C. Sublet, J. Eastwood, J. Morgan, M. Gilbert, M. Fleming, W. Arter, FISPACT-II: an advanced simulation system for activation, transmutation and material modelling, Nuclear Data Sheets 139 (2017) 77–137.
- [23] M. Tosato, M. Verona, C. Favaretto, M. Pometti, G. Zanoni, F. Scopelitti, F. P. Cammarata, L. Morselli, Z. Talip, N. P. van der Meulen, et al., Chelation of theranostic copper radioisotopes with s-rich macrocycles: From radiolabelling of copper-64 to in vivo investigation, Molecules 27 (13) (2022) 4158.
- [24] G. Gilmore, Practical gamma-ray spectroscopy, John Wiley & Sons, 2008.
- [25] C. L. Fontana, M. Lunardon, F. E. Pino, L. Stevanato, A. Carnera, C. Sada, F. Soramel, S. Moretto, A distributed data acquisition system for signal digitizers with on-line analysis capabilities, in: 2017 IEEE Nuclear Science Symposium and Medical Imaging Conference (NSS/MIC), IEEE, 2017, pp. 1–5.
- [26] C. L. Fontana, A. Carnera, M. Lunardon, F. E. Pino, C. Sada, F. Soramel, L. Stevanato, S. Moretto, A distributed data acquisition system for nuclear detectors, in: International Journal of Modern Physics: Conference Series, Vol. 48, World Scientific, 2018, p. 1860118.
- [27] S. Agostinelli, J. Allison, K. a. Amako, J. Apostolakis, H. Araujo, P. Arce, M. Asai, D. Axen, S. Banerjee, G. Barrand, et al., GEANT4—a simulation toolkit, Nuclear instruments and methods in physics research

- 540 section A: Accelerators, Spectrometers, Detectors and Associated Equip-  
ment 506 (3) (2003) 250–303.
- [28] C. M. Poole, I. Cornelius, J. V. Trapp, C. M. Langton, A CAD In-  
terface for GEANT4, Australasian Physical and Engineering Science in  
Medicine (September 2012). doi:10.1007/s13246-012-0159-8.  
545 URL <http://www.springerlink.com/content/u563877422284578>
- [29] P. Andreetto, F. Costa, A. Crescente, S. Fantinel, F. Fanzago, P. E. Maz-  
zon, M. Menguzzato, G. Sella, M. Sgaravatto, S. Traldi, et al., Evolution  
of the cloudveneto. it private cloud to support research and innovation,  
in: EPJ Web of Conferences, Vol. 245, EDP Sciences, 2020, p. 07013.
- 550 [30] J. Blachot, Nuclear data sheets for A= 111, Nuclear Data Sheets 77 (2)  
(1996) 299–432.
- [31] J. Blachot, Nuclear data sheets for A= 109, Nuclear Data Sheets 107 (2)  
(2006) 355–506.



(a)



(b)

Figure 7: Comparison between (a) a picture of the experimental setup and (b) the GEANT4 simulation geometry.

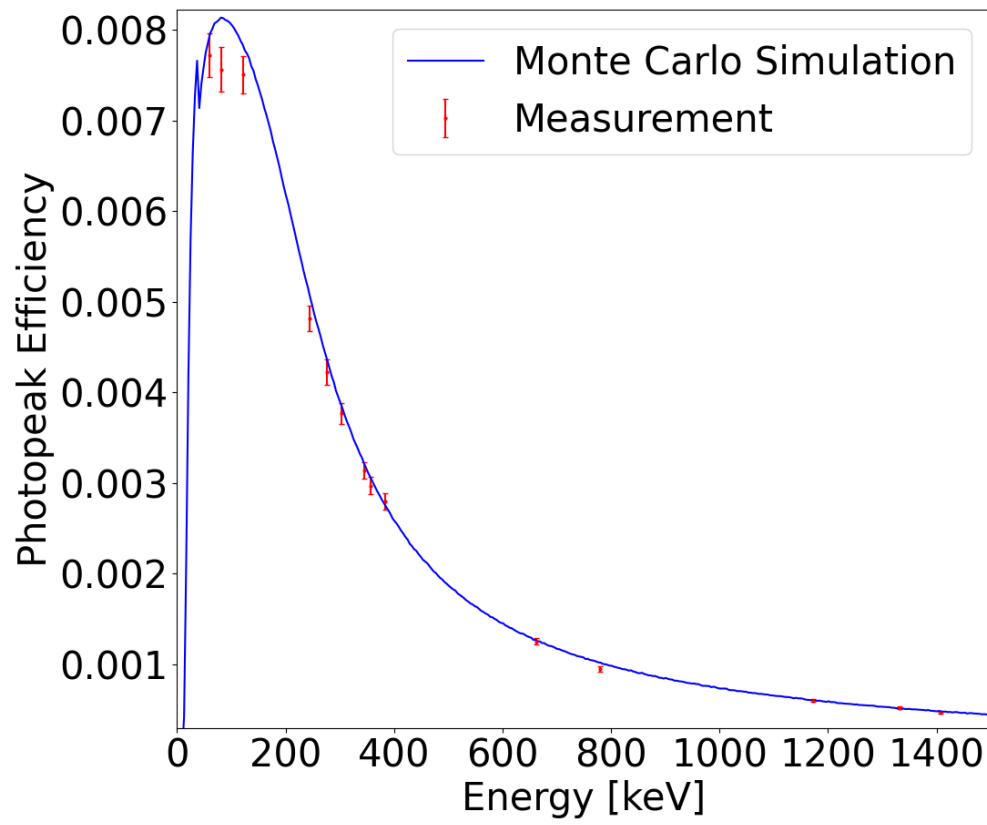


Figure 8: Absolute full energy peak efficiency of the LBC detector estimated by experiments and MC simulations.

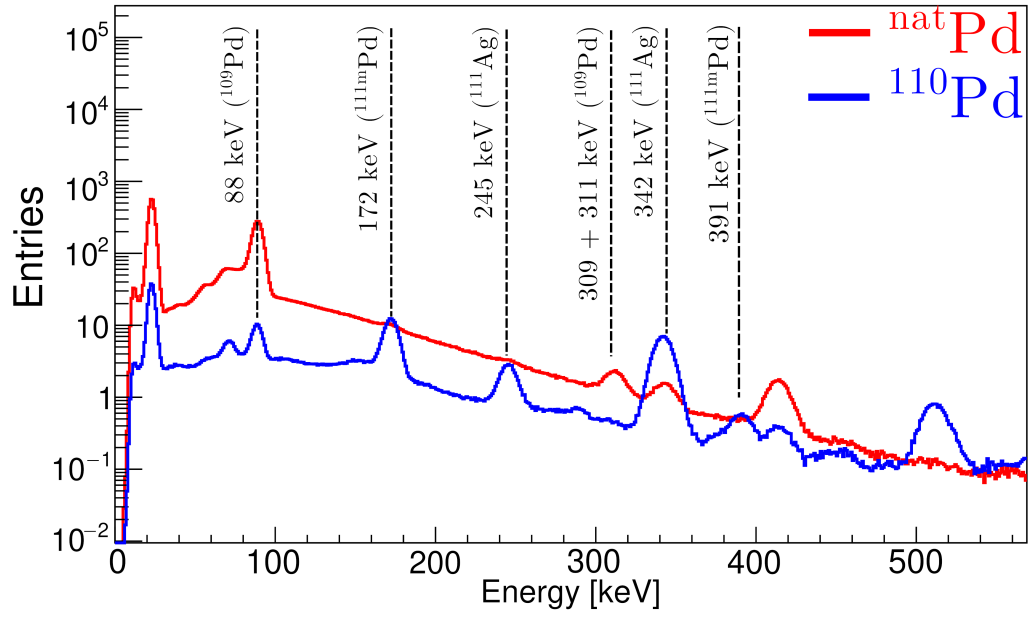


Figure 9:  $\gamma$ -ray spectra of the irradiated  $^{nat}\text{Pd}$  and  $^{110}\text{Pd}$ -enriched samples after 5 hours from the end of the irradiation.

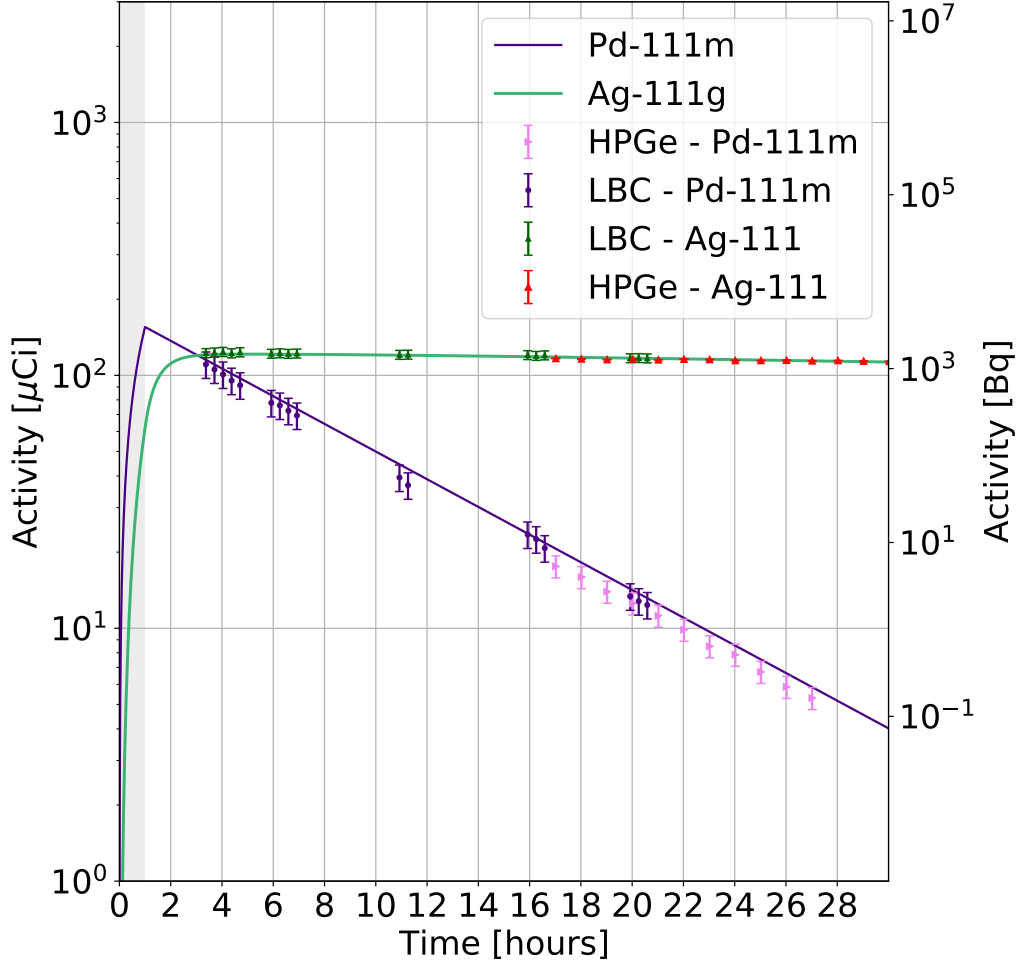


Figure 10: Activities of  $^{111}\text{Ag}$ , measured with LBC (green) and HPGe (red), and of  $^{111\text{m}}\text{Pd}$ , measured with LBC (purple) and HPGe (pink), at different times after the beginning of the irradiation. The solid lines are the solution of the system of ordinary differential equations of Eq. 2 with  $R_{\text{metastable}}/R_{\text{ground}}=4\%$ .

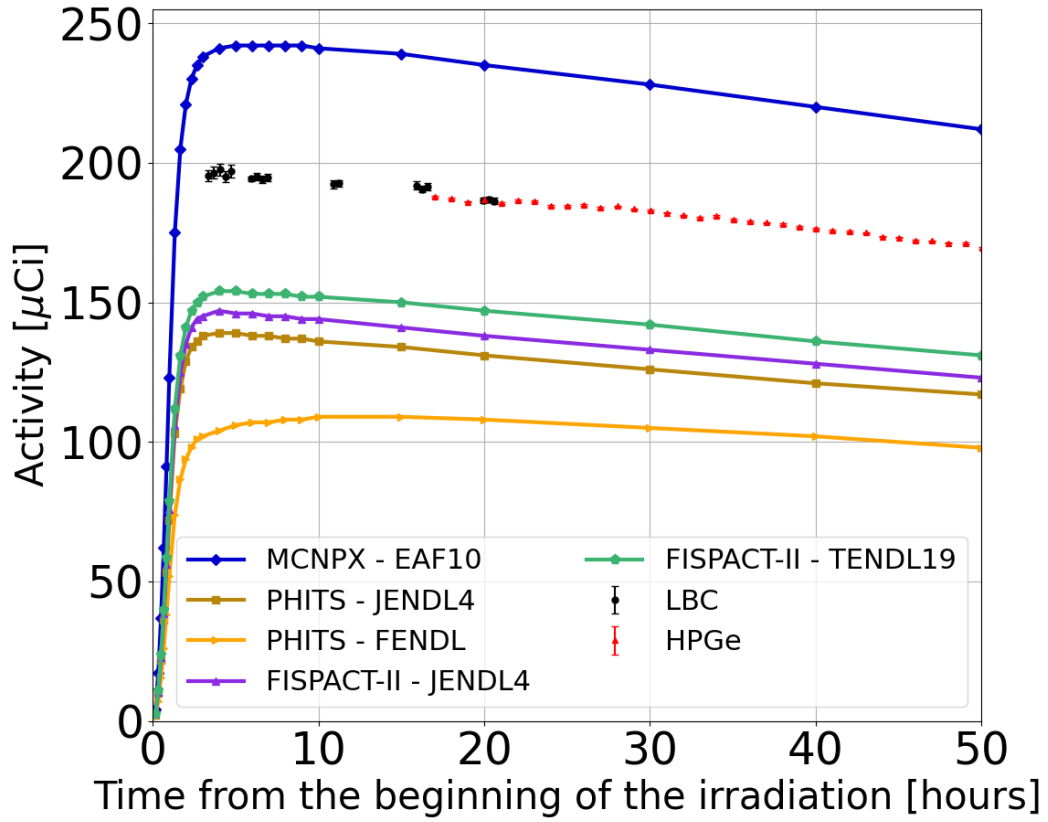


Figure 11: Comparison between measured  $^{111}\text{Ag}$  activity, normalized to a  $^{110}\text{Pd}$ -enriched sample of 100 mg irradiated for one hour in the CT of the TRIGA Mark II reactor, and Monte Carlo simulations with different tools and cross section libraries. Monte Carlo statistical uncertainties are lower than 5%.

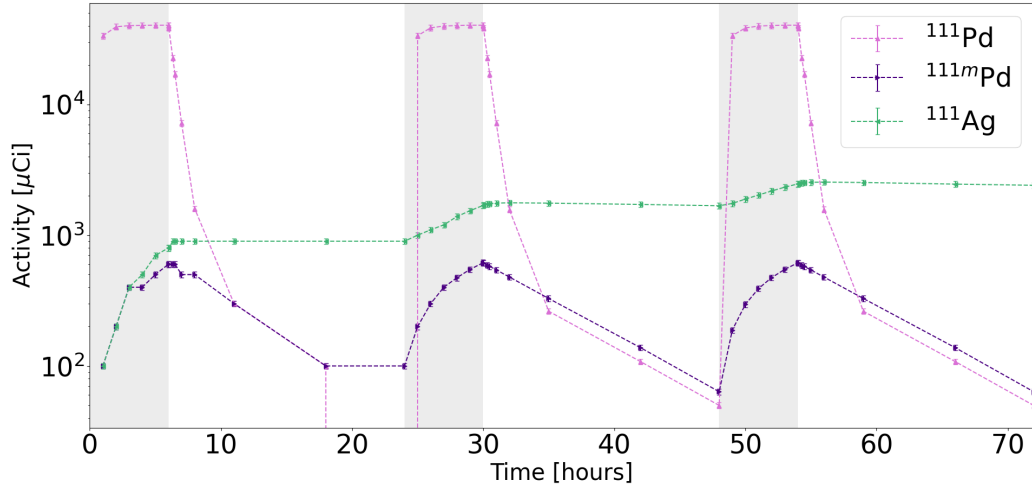


Figure 12: Activities of  $^{111}\text{Pd}$ ,  $^{111m}\text{Pd}$  and  $^{111}\text{Ag}$ , produced irradiating a 100 mg  $^{110}\text{Pd}$ -enriched sample in the CT of the TRIGA Mark II reactor at full power. Activities are plotted as a function of time after the beginning of the irradiation. A duty cycle of the TRIGA Mark II reactor of 6 hours a day is assumed. Irradiation periods are highlighted in grey. Calculations are performed using FISPACT-II with the TENDL-2019 cross section library. Monte Carlo statistical uncertainties are lower than 5%.